

# Search for supersymmetry in diphoton final states with the CMS detector

Matthew Lawrence Joyce

March 18, 2021

## CONTENTS

1.	<i>The Standard Model</i>	7
2.	<i>Supersymmetry</i>	8
3.	<i>The Large Hadron Collider</i>	9
3.1	Introduction	9
3.2	Injection Complex	9
3.3	Tunnel and Magnets	10
3.4	Luminosity	12
4.	<i>Compact Muon Solenoid</i>	14
4.1	Introduction	14
4.2	Coordinate System	15
4.3	Tracker	16
4.3.1	Pixel Detector	16
4.3.2	Strip Detector	17
4.4	Electromagnetic Calorimeter	18
4.4.1	Crystals	19
4.4.2	Barrel and Endcaps	19
4.4.3	Preshower layer	21
4.4.4	Performance	21
4.5	Hadronic Calorimeter	22
4.6	Superconducting Solenoid	23
4.7	Muon System	23
5.	<i>MIP Timing Detector (MTD)</i>	26
5.1	Introduction	26
5.2	Barrel Timing Layer	27
6.	<i>CMS Trigger System</i>	29
6.1	L1 trigger	29
6.1.1	Calorimeter trigger	29

6.1.2	Muon trigger . . . . .	30
6.1.3	Global Trigger . . . . .	31
6.2	High Level Trigger . . . . .	31
6.3	Trigger efficiency . . . . .	31
7.	<i>CMS Particle and Event Reconstruction</i> . . . . .	32
7.1	Tracks . . . . .	32
7.2	Calorimeter clusters . . . . .	33
7.3	Object identification . . . . .	33
7.3.1	Muons . . . . .	33
7.3.2	Electrons . . . . .	34
7.3.3	Photons . . . . .	35
7.3.4	Jets . . . . .	35
7.4	Missing transverse momentum . . . . .	35
8.	<i>Data Analysis</i> . . . . .	36
8.1	Overview . . . . .	36
8.2	Data sets . . . . .	36
8.3	Object definitions . . . . .	36

## LIST OF FIGURES

3.1	LHC interaction points . . . . .	10
3.2	Layout of LHC accelerator complex [16]. . . . .	11
3.3	Proton bunch capture onto RF bucket [6]. . . . .	12
3.4	Cross section of LHC dipole [9] . . . . .	13
3.5	Integrated luminosity delivered by the LHC to the CMS experiment each year from 2010-2018. . . . .	13
4.1	Schematic of CMS detector [19] . . . . .	14
4.2	Transverse slice of the CMS detector[7]. . . . .	15
4.3	Cross section (side) of CMS tracker prior to the Phase 1 upgrade during the year-end technical stop of 2016/2017. Each line represents a detector module while double lines indicate back-to-back strip modules. Surrounding the pixel tracker (PIXEL) is the strip detector, which is divided into the Tracker Inner Barrel (TIB), Tracker Outer Barrel (TOB), Tracker Inner Disks (TID), and Tracker Endcaps (TEC). Reprinted from Reference [12]. . . . .	17
4.4	Cross section (side) of pixel detector. The lower half , labeled "Current", shows the design prior to 2017 while the upper half, labeled "Upgrade", shows the design after the upgrade. Reprinted from Resource [11] . . . . .	18
4.5	PbWO <sub>4</sub> crystals. Left: EB crystal with APD. Right: EE crystal with VPT. Reprinted from [13] . . . . .	20
4.6	Schematic of ECAL. Reprint from [13] . . . . .	21
4.7	Longitudinal view of HCAL [2] . . . . .	23
4.8	Longitudinal slice of CMS detector while operating at 3.8-T central magnetic field. The right-hand side of the figure shows a mapping of the magnetic field lines while the left-hand side shows a mapping of the field strength. Reprint from [10] . . .	24

4.9	Cross-section of one quadrant of the CMS detector. The DTs are labeled as "MB" (Muon Barrel) and the CSCs are labelled as "ME" (Muon Endcap). The RPCs are "RB" for those in the barrel and "RE" for those in the endcap. Reprint from [20].	25
5.1	Timeline for LHC . . . . .	26
5.2	Vertices from a simulated 200 pileup event. Need to replace this with the figure from the TDR. . . . .	27
6.1	L1 trigger system. Reprint from [3] . . . . .	30
7.1	Effect of Bremsstrahlung . . . . .	35

## LIST OF TABLES

4.1	Summary of signals expected for each particle type in each sub-detector. . . . .	15
6.1	Primary HLT . . . . .	31

## 1. THE STANDARD MODEL

## 2. SUPERSYMMETRY

3                   3. THE LARGE HADRON COLLIDER

4                   3.1 *Introduction*

5     The Large Hadron Collider (LHC) is a 26.7 kilometer-long, two-ring particle  
6     accelerator and collider located on the border of France and Switzerland at  
7     the European Organization for Nuclear Research (CERN). During normal  
8     operations the LHC maintains two counter-rotating beams of proton bunches  
9     that collide at four interaction points (IP) with up to  $\sqrt{s} = 14$  TeV center  
10    of mass energy and a luminosity of  $10^{34}\text{cm}^{-2}\text{s}^{-1}$ . The ALICE (Point 2),  
11    ATLAS (Point 1), CMS (Point 5), and LHC-b experiments each have a  
12    detector at one of these interaction points as scene in Figure 3.1 . The CMS  
13    and ATLAS are general-purpose detectors while LHC-b specializes in beauty  
14    quark studies. ALICE is a heavy-ion experiment which uses  $^{208}\text{Pb} - p$  or  
15     $^{208}\text{Pb} - ^{208}\text{Pb}$  collisions that can also be produced by the LHC.

16                  3.2 *Injection Complex*

17    In order to bring the protons from rest up to their target collision energy  
18    a series of accelerators, as shown in Figure 3.2, are used. The acceleration  
19    sequence begins with the injection of hydrogen gas into a duoplasmatron.  
20    Here a bombardment of electrons ionize the hydrogen atoms while an electric  
21    field pushes them through the duoplasmatron cavity. The result is 100 keV  
22    protons being passed on to a quadrupole magnet which guides them into  
23    the aperture of a linear accelerator (LINAC2). The radio frequency (RF)  
24    cavities in LINAC2 accelerate the protons up to 50 MeV. At this point the  
25    protons are sent into one of four rings in the Proton Synchrotron Booster  
26    (PSB). The PSB repeatedly accelerates the protons around a circular path  
27    until they reach an energy of 1.4 GeV. The bunches of protons from each PSB  
28    ring are then sequentially injected into the single-ringed Proton Synchrotron  
29    (PS). Each bunch injected into the PS are captured by one of the "buckets"  
30    (Figure 3.3) provided by the PS RF system which also manipulates the  
31    bunches into the desired profile and proton density. These proton bunches  
32    are accelerated to 25 GeV and injected into the Super Proton Synchrotron

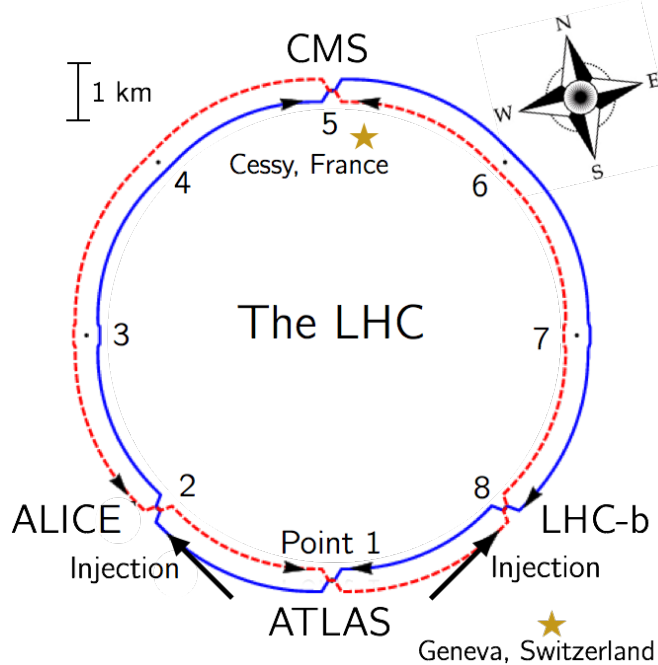


*Fig. 3.1: Interaction points of the LHC*

<sup>33</sup> (SPS) where they are accelerated to 450 GeV. Finally the proton bunches  
<sup>34</sup> are injected into the LHC ring where they are accelerated to 6.5 TeV and  
<sup>35</sup> collided in 25 ns intervals to yield a center of mass energy of  $\sqrt{s} = 13$  TeV.

### <sup>36</sup> 3.3 Tunnel and Magnets

<sup>37</sup> The LHC was designed to produce collisions with up to  $\sqrt{s} = 14$  TeV. That  
<sup>38</sup> requires confining and guiding 7 TeV protons around the circumference of  
<sup>39</sup> the LHC ring. The ring is housed in a 4 meter-wide underground tunnel  
<sup>40</sup> that ranges in depth between 45 and 170 meters below the surface. This  
<sup>41</sup> tunnel was repurposed from the Large Electron-Positron (LEP) Collider  
<sup>42</sup> which previously occupied the space. For this reason the tunnel is not  
<sup>43</sup> completely circular but is instead made up of alternating curved and straight  
<sup>44</sup> sections of 2500 m and 530 m in length respectively. The straight sections,  
<sup>45</sup> labeled 1-8 in Figure 3.1, are used as either experimental facilities or sites for  
<sup>46</sup> hardware necessary for LHC operations such as RF cavities for momentum  
<sup>47</sup> cleaning, quadrupole magnets for beam focusing, and sextupole magnets for  
<sup>48</sup> acceleration and betatron cleaning.

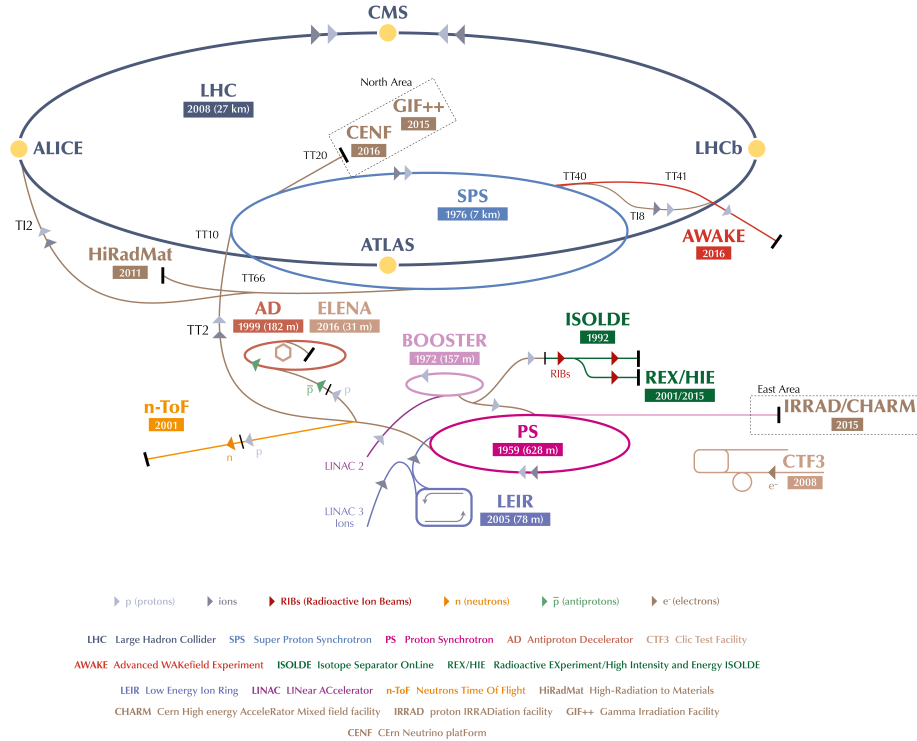


Fig. 3.2: Layout of LHC accelerator complex [16].

49     Steering a 7 TeV proton beam around the curved sections requires a mag-  
50     netic field of 8.33 Tesla which is provided by 1223 superconducting dipole  
51     magnets cooled to 1.9 K. A cross section of the LHC dipole is shown in  
52     Figure 3.4. Supercooled liquid helium flows through the heat exchanger  
53     pipe to cool the iron yolk to a temperature of 1.9 K. Ultra high vacuum  
54     is maintained in the outer volume to provide a layer of thermal insulation  
55     between the inner volume and the outer steel casing. Inside the iron yolk is a  
56     twin bore assembly of niobium-titanium superconducting coils. Two parallel  
57     beam pipes are located within the focus of the superconducting coils. This  
58     is the ultra high vacuum region where the subatomic particles are confined  
59     as they travel around the LHC ring.

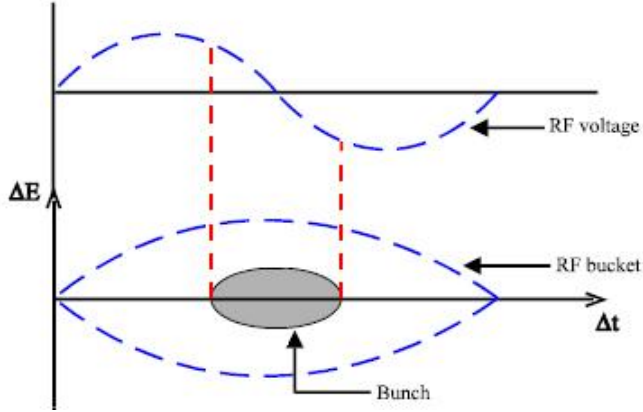


Fig. 3.3: Proton bunch capture onto RF bucket [6].

### 3.4 Luminosity

61 The number of events generated per second for specific process having cross-  
62 section  $\sigma_{event}$  is given by:

$$\frac{dN_{event}}{dt} = L\sigma_{event} \quad (3.1)$$

63 where  $L$  is the machine luminosity. The machine luminosity for a Gaussian  
64 beam distribution can be written in terms of the beam parameters as:

$$L = \frac{N_b^2 n_b f_{rev} \gamma_r}{4\pi \epsilon_n \beta_*} F \quad (3.2)$$

65 where  $N_b$  is particle density in each bunch,  $n_b$  is the number of bunches  
66 in each beam,  $f_{rev}$  is the frequency of revolution, and  $\gamma_r$  is the relativistic  
67 gamma factor. The variables  $\epsilon_n$  and  $\beta_*$  are the normalized transverse beam  
68 emittance and the beta function at the IP respectively, while  $F$  is the geo-  
69 metric reduction factor depending due to the beams' crossing angle at the  
70 IP. [16]

71 The total number of events produced over a given amount of time would  
72 then be

$$N_{event} = \sigma_{event} \int L dt = \sigma_{event} L_{integrated}. \quad (3.3)$$

73 The integrated luminosity delivered each year to the CMS experiment is  
74 shown in 3.5. The analysis presented here uses data collected from the 2016,  
75 2017, and 2018 campaigns which gives a combined integrated luminosity of  
76  $158.7 \text{ fb}^{-1}$ .

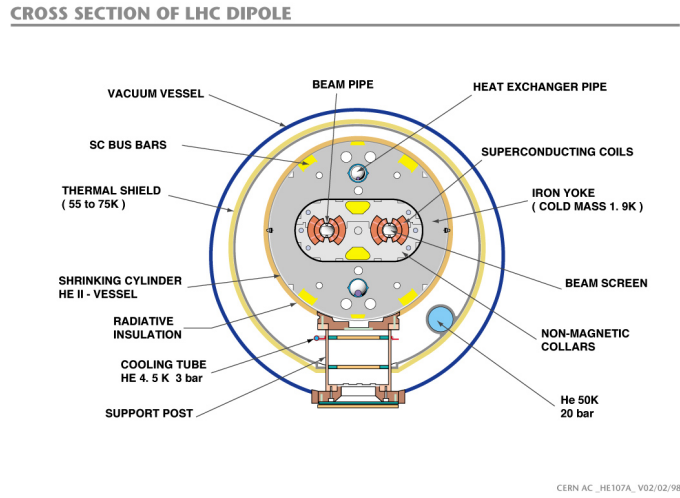


Fig. 3.4: Cross section of LHC dipole [9]

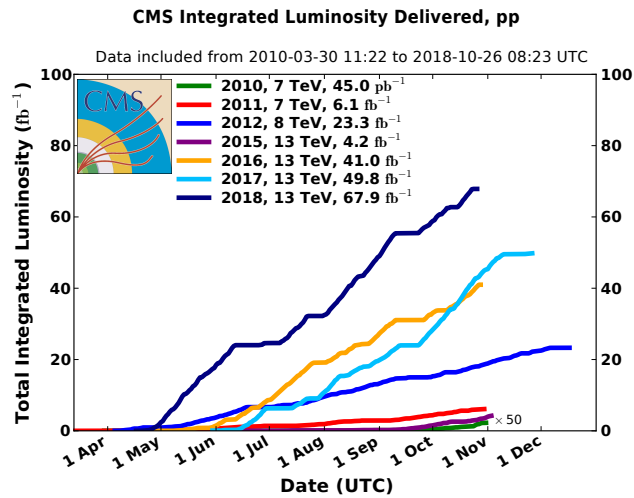
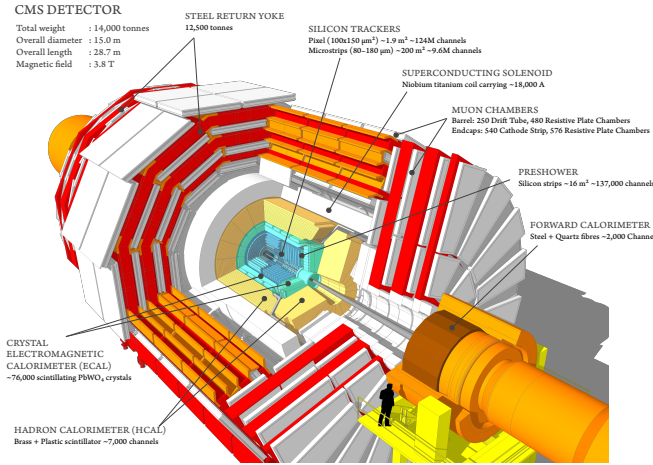


Fig. 3.5: Integrated luminosity delivered by the LHC to the CMS experiment each year from 2010-2018.

## 4. COMPACT MUON SOLENOID

### 4.1 Introduction

79 About 100 meters below the town of Cessy, France at Point 5 is the Compact  
 80 Muon Solenoid (CMS). The CMS is a general purpose detector weighing  
 81 14,000 tonnes with a length of 28.7 meters and a 15.0-meter diameter that  
 82 was designed to accurately measure the energy and momentum of particles  
 83 produced in the proton-proton or heavy-ion collisions at the LHC [13]. A  
 84 perspective view of the detector is shown in Figure 4.1. In order to get  
 85 a full picture of what is being produced by the collisions the CMS detector  
 86 must be able identify the resulting particles as well as accurately measure  
 87 their energy and momentum. For this reason the detector was designed to  
 88 be a collection of specialized sub-detectors, each of which contributes data  
 used in the reconstruction of a collision.



*Fig. 4.1: Schematic of CMS detector [19]*

90 At the heart of the CMS detector is a 3.8-Tesla magnetic field produced  
 91 by a superconducting solenoid. Inside the 6-meter diameter solenoid are

three layers of sub-detectors. These make up the inner detector and are, in order from innermost to outermost, the silicon tracker, the electromagnetic calorimeter (ECAL), and the hadronic calorimeter (HCAL). Outside the solenoid is the muon system. A transverse slice of the detector (Figure 4.2) shows the sub-detectors and how different types of particles interact with them. Table 4.1 shows a summary of which sub-detectors are expected to produce signals for different types of particles.

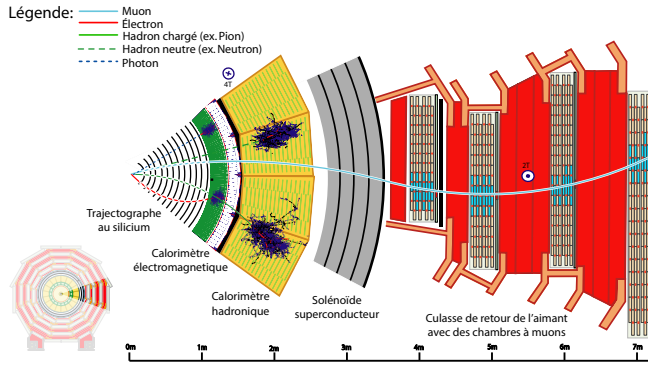


*Fig. 4.2:* Transverse slice of the CMS detector[7].

Particle	Tracker	ECAL	HCAL	Muon
Photons	No	Yes	No	No
Electrons	Yes	Yes	No	No
Hadrons (charged)	Yes	Yes	Yes	No
Hadrons (neutral)	No	No	Yes	No
Muons	Yes	Yes	Yes	Yes
Invisible ( $\nu$ , SUSY, etc)	No	No	No	No

*Tab. 4.1:* Summary of signals expected for each particle type in each sub-detector.

## 4.2 Coordinate System

The origin of the coordinate system used by CMS is centered at the nominal collision point in the center of the detector. A right-handed Cartesian system is used with the x-axis pointing radially inward toward the center of the LHC ring, y-axis pointing vertically upward, and the z-axis pointing tangent to

104 the LHC ring in the counterclockwise direction as viewed from above. CMS  
 105 also uses an approximately Lorentz invariant spherical coordinate system  
 106 spanned by three basis vectors. They are the transverse momentum  $p_T$ ,  
 107 pseudorapidity  $\eta$ , and azimuthal angle  $\phi$ . The transverse momentum and  
 108 azimuthal angle translate to the Cartesian system in the following ways  
 109 using the x and y-components of the linear momentum:

$$p_T = \sqrt{(p_x)^2 + (p_y)^2} \quad (4.1)$$

$$\phi = \tan^{-1} \frac{p_y}{p_x} \quad (4.2)$$

110 while the pseudorapidity can be translated using the polar angle  $\theta$  relative  
 111 the positive z-axis as

$$\eta = -\ln[\tan \frac{\theta}{2}] \quad (4.3)$$

### 113 4.3 Tracker

114 The innermost sub-detector in CMS is the silicon tracker. The tracker is  
 115 used to reconstruct tracks and vertices of charged particles. In order to give  
 116 precise reconstruction of charged particle trajectories it needs to be position  
 117 as close as possible to the IP and have high granularity. The close proximity  
 118 to the IP requires the materials to be tolerant to the high levels of radiation  
 119 in that region. Being the innermost sub-detector it must also minimally  
 120 disturb particles as they pass through it into the other sub-detectors. These  
 121 criteria led to the design of the tracker using silicon semiconductors.

122 The silicon tracker is made up of two subsystems, an inner pixel detector  
 123 and an outer strip tracker which are oriented in a cylindrical shape with an  
 124 overall diameter of 2.4 m and length of 5.6 m centered on the interaction  
 125 point. Both subsystems consist of barrel and endcap regions which can be  
 126 seen in Figure 4.3.

#### 127 4.3.1 Pixel Detector

128 The pixel detector is the innermost subsystem in the silicon tracker and  
 129 spans the pseudorapidity range  $|\eta| < 2.5$  and is responsible for small im-  
 130 pact parameter resolution which is important for accurate reconstruction of  
 131 secondary vertices [13]. In order to produce these precise measurements a  
 132 very high granularity is required. In addition to this the proximity to the  
 133 IP means that one expects there to be high occupancy of the tracker. These  
 134 constraints are met by using pixels with a cell size of  $100 \times 150 \mu\text{m}^2$ .

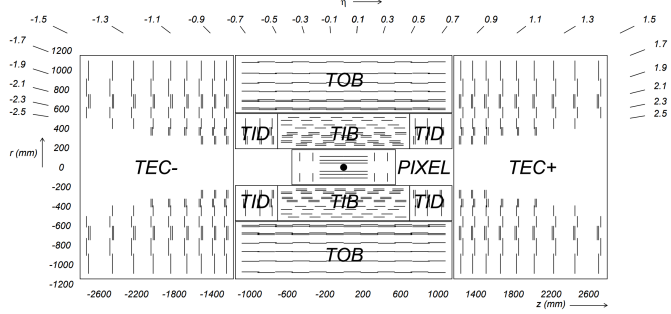


*Fig. 4.3:* Cross section (side) of CMS tracker prior to the Phase 1 upgrade during the year-end technical stop of 2016/2017. Each line represents a detector module while double lines indicate back-to-back strip modules. Surrounding the pixel tracker (PIXEL) is the strip detector, which is divided into the Tracker Inner Barrel (TIB), Tracker Outer Barrel (TOB), Tracker Inner Disks (TID), and Tracker Endcaps (TEC). Reprinted from Reference [12].

135 The original pixel detector was designed for operation at the nominal  
 136 instantaneous luminosity of  $10^{34} \text{ cm}^{-2}\text{s}^{-1}$  with 25 ns between proton bunch  
 137 crossings, resulting in on average about 25 proton-proton interactions occur-  
 138 ring per bunch crossing or pileup [12]. During the LHC technical shutdown  
 139 of 2016/17, the pixel detector underwent the scheduled Phase 1 upgrade  
 140 which would allow operation at higher levels of instantaneous luminosity  
 141 and pileup. Figure 4.4 shows a cross sectional view in the  $r$ - $z$  plane. Prior  
 142 to 2017 there were three barrel layers and two endcap layers on each side  
 143 which provide three very precise space points for each charged particle. The  
 144 upgrade decreased the radius of the innermost barrel layer from 4.4 cm to  
 145 3.0 cm and added a fourth barrel layer as well as adding third endcap layer  
 146 to each side. Each of the endcap layers consisted of two half-disks populated  
 147 with pixel modules whereas the upgraded endcap layers were split into inner  
 148 and outer rings. [11]

#### 149           4.3.2 Strip Detector

150 The silicon strip detector surrounds the pixel detector and is comprised of  
 151 four subsystems, the Tracker Inner Barrel (TIB), the Tracker Outer Barrel  
 152 (TOB), the Tracker Inner Disks (TID), and the Tracker Endcaps (TEC),  
 153 all of which can be seen in Figure 4.3 [13]. The TIB and TID both use  
 154 320  $\mu\text{m}$  thick silicon micro-strip sensors oriented along  $z$  and  $r$  respectively.  
 155 The TIB has four layers while the TID is composed of three layers. This

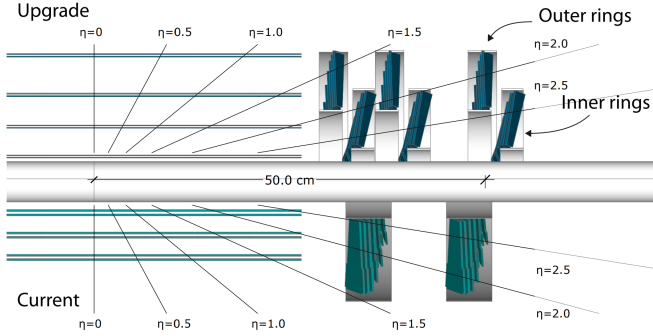


Fig. 4.4: Cross section (side) of pixel detector. The lower half , labeled "Current", shows the design prior to 2017 while the upper half, labeled "Upgrade", shows the design after the upgrade. Reprinted from Resource [11]

geometry allows the TIB and TID to combine to provide up to four  $r - \phi$  measurements on charged particle trajectories.

Surrounding the TIB and TID is the TOB, which extends between  $z \pm 118$  cm. This subsystem consists of six layers of 500  $\mu\text{m}$  thick silicon micro-strip sensors with strip pitches ranging from 122  $\mu\text{m}$  to 183  $\mu\text{m}$ , providing six more  $r - \phi$  measurements in addition to those from the TIB/TID subsystems. Beyond the  $z$  range of the TOB is the TEC. Each TEC is made up of nine disks. Each of the nine disks has up to seven concentric rings of micro-strip sensors oriented in radial strips with those on the inner four rings being 320  $\mu\text{m}$  thick and the rest being 500  $\mu\text{m}$  thick, providing up to nine  $\phi$  measurements for the trajectory of a charged particle.

To provide additional measurements of the  $z$  coordinate in the barrel and  $r$  coordinate in the disks a second micro-strip detector module is mounted back-to-back with stereo angle 100 mrad in the first two layers of the TIB and TOB, the first two rings of the TID, and rings 1, 2, and 5 of the TEC. The resulting single point resolution is 230  $\mu\text{m}$  in the TIB and 530  $\mu\text{m}$  in the TOB. The layout of these subsystems ensures at least nine hits for  $|\eta| < 2.4$  with at least four of hits yielding a 2D measurement.

#### 4.4 Electromagnetic Calorimeter

The electromagnetic calorimeter (ECAL) lies just outside the tracker and is a hermetic homogeneous calorimeter designed to measure the energy deposited by electrons and photons. It consists of a central barrel (EB) with 61200 lead tungstate ( $\text{PbWO}_4$ ) crystals which is closed by two endcaps (EE), each

179 having 7324 crystals. Highly-relativistic charged particles passing through a  
180 crystal primarily lose energy by producing bremsstrahlung photons. Photons  
181 lose energy by producing  $e^- - e^+$  pairs. In front of each EE is a preshower  
182 (ES) detector which acts as a two-layered sampling calorimeter. The crystals  
183 in the EB are instrumented with avalanche photodiodes (APDs) while the  
184 EE crystals are instrumented with vacuum phototriodes (VPTs). The ECAL  
185 design was strongly driven to be sensitive to the di-photon decay channel  
186 of the Higgs boson. This led to the design of a calorimeter that was fast,  
187 radiation-hard, and had good spatial and energy resolution.

188                   4.4.1 Crystals

189 In order to provide a good spacial resolution it was necessary for the ECAL  
190 to have a fine granularity. The small Molier radius (22 mm) and short radia-  
191 tion length (8.9 mm) of PbWO<sub>4</sub> allows for fine granularity while maintaining  
192 good energy resolution by containing nearly all of the energy from an EM  
193 shower without the need for a restrictively thick crystal layer. The PbWO<sub>4</sub>  
194 scintillation is also fast enough that approximately 80 percent of an EM  
195 shower is produced within 25 ns, which is the also the amount of time be-  
196 tween bunch crossings at the LHC. These crystals have a Gaussian-shaped  
197 spectrum spanning from 360 nm to 570 nm with a maximum at approx-  
198 imately 440 nm. While PbWO<sub>4</sub> is relatively radiation-hard, the amount  
199 of ionizing radiation seen by the crystal leading up to the HL-LHC era of  
200 operations causes wavelength-dependent degradation in light transmission.  
201 The scintillation mechanism however is unchanged so this damage can be  
202 tracked and accounted for by injecting laser light near the peak wavelength  
203 of the emission spectrum into the crystals to monitor optical transparency.

204 Light produced in the crystal is transmitted along its length and col-  
205 lected at the rear by either an APD in the EB or a VPT in one of the EE.  
206 Light output is temperature dependent so the crystals are kept at precisely  
207 18°C at which the yield is about 4.5 photoelectrons per MeV. The EB and  
208 EB crystals, which have a tuncated pyramidal shape to match the lateral de-  
209 velopment of the shower, along with their photosensors are shown in Figure  
210 4.5.

211                   4.4.2 Barrel and Endcaps

212 The EB covers the pseudorapidity range  $|\eta| < 1.479$  and uses crystals that  
213 are 230 mm long, which corresponds to 25.8 radiation lengths. The front  
214 face of each crystal measures  $22 \times 22$  mm<sup>2</sup> while the rear face measures  $26 \times 26$

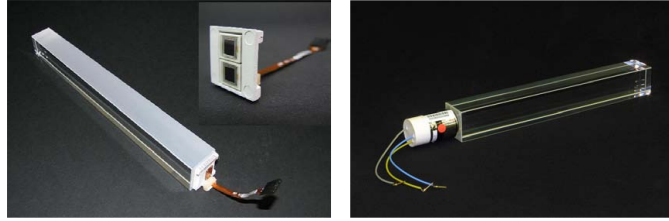


*Fig. 4.5:* PbWO<sub>4</sub> crystals. Left: EB crystal with APD. Right: EE crystal with VPT. Reprinted from [13]

mm<sup>2</sup>. These are grouped in 36 supermodules (SM), each comprised of 1700 crystals arranged in a 20×85 grid in  $\phi \times \eta$ . Each SM spans half the length of the barrel and covers 20° in  $\phi$ . On the back face of each crystal is a pair of APDs (semiconductor diodes). APDs are compact, immune to the longitudinal 3.8 T magnetic field produced by the solenoid at this location, and resistant to the radiation levels expected in the EB over a ten year period. They also have high enough gain to counter to low light yield of the crystals. All of this makes them an ideal choice for use in the EB. Each APD has an active area of 5 × 5 mm<sup>2</sup> and are operated at a gain of 50 which requires a bias voltage between 340 and 430 V. As the gain of the APDs is highly dependent on the applied bias voltage and any gain instability would translate to degradation in energy resolution, very stable power supplies are used to maintain voltages within a few tens of mV.

The EE cover the pseudorapidity range 1.497 < | $\eta$ | < 3.0. The crystals in the EE have a 28.62×28.62 mm<sup>2</sup> front face cross section and 30×30 mm<sup>2</sup> rear face cross section. Each crystal is 220 mm long which corresponds to 24.7 radiation lengths and are grouped in 5×5 units called supercrystals (SCs). Two halves, called *Dees*, make up each EE. Each Dee contains 138 SCs and 18 partial SCs which lie along the inner and outer circumference. On the back of each crystal in EE is a VPT which is a conventional photomultiplier with a single gain stage. While not as compact as the APDs used in the EB, the VPTs are a more suitable for the more hostile environment at higher  $\eta$ . Each VPT has a 25-mm diameter and approximately 280 mm<sup>2</sup> of active area. Though the VPT gain and quantum efficiency are lower than that of the APDs this is offset by the larger active area allowing for better light collection. Figure 4.6 shows the orientation of the crystals, modules, and supermodules within the ECAL. [13]

242

#### 4.4.3 Preshower layer

243 In front of each EE is a preshower (ES) detector. The main purpose of the  
 244 ES is to identify photons resulting from  $\pi^0 \rightarrow \gamma\gamma$  within the pseudorapidity  
 245 range  $1.653 < |\eta| < 2.6$ , but it also aids in the identification of electrons  
 246 against minimum ionizing particles (MIPs) and provides a spacial resolution  
 247 of 2 mm compared to the 3 mm resolution of the EB and EE. The ES acts  
 248 as a two-layered sampling calorimeter. Lead radiators make up the first  
 249 layer. These initiate electromagnetic showers from incoming electrons or  
 250 photons. The deposited energy and transverse profiles of these showers are  
 251 then measured by the silicon strip sensors which make up the second layer.

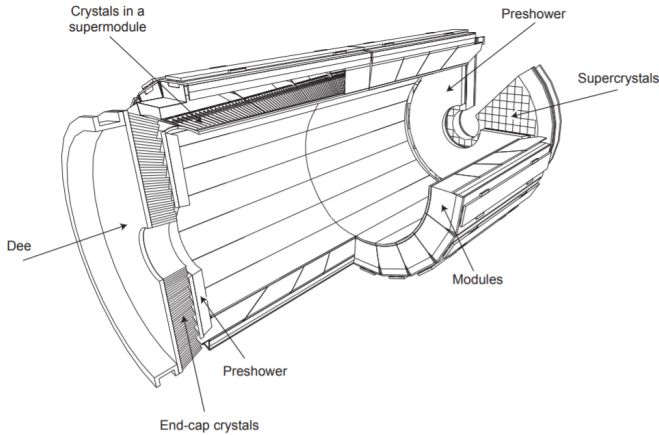


Fig. 4.6: Schematic of ECAL. Reprint from [13]

252

#### 4.4.4 Performance

253 The energy resolution of the ECAL can be parameterized as

$$\frac{\sigma}{E} = \frac{S}{\sqrt{E}} \oplus \frac{N}{E} \oplus C \quad (4.4)$$

254 where  $S$  is the stochastic term characterizing the size of photostatistical  
 255 fluctuations,  $N$  is the term characterizing the contributions of electronic,  
 256 digital, and pileup noise, and  $C$  is a constant which accounts for crystal  
 257 performance non-uniformity, intercalibration errors, and leakage of energy  
 258 from the back of a crystal. The values for these terms, as measured in a  
 259 beam test using 20 to 250 GeV electrons, are  $S = 0.028 \text{ GeV}^{1/2}$ ,  $N = 0.12$   
 260 GeV, and  $C = 0.003$ . [13]

---

 261        4.5 Hadronic Calorimeter

262     In the space between the bore of the superconducting magnet and the ECAL  
 263     is the Hadronic Calorimeter (HCAL) [2]. The HCAL is a sampling calorime-  
 264     ter used for the measurement of hadronic jets and apparent missing trans-  
 265     verse energy resulting from neutrinos or exotic particles. It is made up of al-  
 266     ternating layers of plastic scintillator tiles and brass absorbers. EM showers  
 267     are generated by charged/neutral hadrons in the brass absorber. Charged  
 268     particles in the shower then produce scintillation light in the plastic scintil-  
 269     lator. Wavelength-shifting optical fibers embedded in the scintillator collect  
 270     and guide the scintillation light to pixelated hybrid photodiodes. A longi-  
 271     tudinal cross-section view in Figure 4.7 shows the geometric layout of the  
 272     HCAL’s barrel (HB), outer barrel (HO), endcap (HE), and forward (HF)  
 273     sections. The HB is comprised of 17 scintillator layers extending from 1.77  
 274     to 1.95 m and covers the pseudorapidity range of  $|\eta| < 1.4$ . The HO lies  
 275     outside the solenoid and is composed of only scintillating material. This  
 276     increases the interaction depth of the calorimeter system to a minimum of  
 277      $11\lambda_I$  for  $|\eta| < 1.26$  and thus reduces energy leakage. Also located inside  
 278     the solenoid are the two HE which cover pseudorapidities  $1.3 < |\eta| < 3.0$   
 279     and provide a thickness of  $10\lambda_I$ . In the forward region is the HF. This is  
 280     located 11.2 m away from the IP and covers the  $2.9 < |\eta| < 5.2$ . As the  
 281     HF is exposed to the highest levels of particle flux, it uses quartz fibers em-  
 282     bedded in steel absorbers rather than the materials used in the other parts  
 283     of the HCAL. Showers initiated by the absorbers produce Cerenkov light  
 284     in the quartz which transmits along to the fibers to photomultiplier tubes  
 285     (PMTs).

286     The HCAL inherently has lower energy resolution than the ECAL. A  
 287     large portion of the energy from hadronic showers is deposited in the ab-  
 288     sorbers and never makes it to the scintillation material. There are also  
 289     the possibilities that showers can be initiated prior to the particles reach-  
 290     ing HCAL or a charged particle could deposit energy in the ECAL through  
 291     bremsstrahlung. The combined energy resolution of the ECAL and the  
 292     HCAL barrels can be parameterized as

$$\frac{\sigma}{E} = \frac{S}{\sqrt{E}} \oplus C, \quad (4.5)$$

293     where  $E$  is the energy of the incident particle. These quantities were mea-  
 294     sured in a beam test using 2 to 350 GeV/c hadrons, electrons, and muons.  
 295     The stochastic term is  $S = 0.847 \text{ GeV}^{1/2}$ , and the constant term is  $C = 0.074$   
 296     [4].

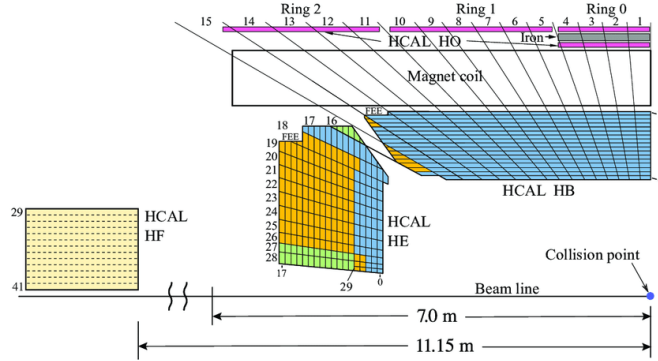


Fig. 4.7: Longitudinal view of HCAL [2]

297

#### 4.6 Superconducting Solenoid

298 In between the HCAL barrel and outer barrel is the superconducting solenoid  
 299 magnet. The magnet is 12 m long with a 6-m inner diameter and provides  
 300 the bending power necessary to precisely measure the momentum of charged  
 301 particles. While it is capable of producing a 4 T magnetic field, the magnet  
 302 is typically operated at 3.8 T. This is done to prolong the lifetime of the  
 303 magnet. The Niobium Titanium coils used to create the uniform 3.8-T  
 304 magnetic field are suspended in a vacuum cryostat and cooled by liquid helium  
 305 to a temperature of 4.5 K. The magnet has a stored energy of 2.6 GJ when  
 306 operating at full current. There are five wheels in the barrel and three  
 307 disks on each endcap that make up a 12,000 ton steel yoke which serves to  
 308 return the magnetic flux. This, along with a mapping of the calculated field  
 309 strength, can be seen in Figure 4.8. More details on the superconducting  
 310 solenoid magnet can be found at [1]

311

#### 4.7 Muon System

312 Embedded in magnet return yoke and encapsulating all of the other sub-  
 313 detectors is the muon system. The muon system is the outermost layer  
 314 because muons don't interact via the strong force and electromagnetic in-  
 315 teractions alone are not enough to stop them due to their large mass, therefore  
 316 the only particles that are capable of making it to the muon system are  
 317 muons and weakly-interacting particles such as neutrinos. The muon sys-  
 318 tem is comprised of three different types of detectors. These are drift tube  
 319 (DT) chambers, cathode strip chambers (CSC), and resistive plate chambers

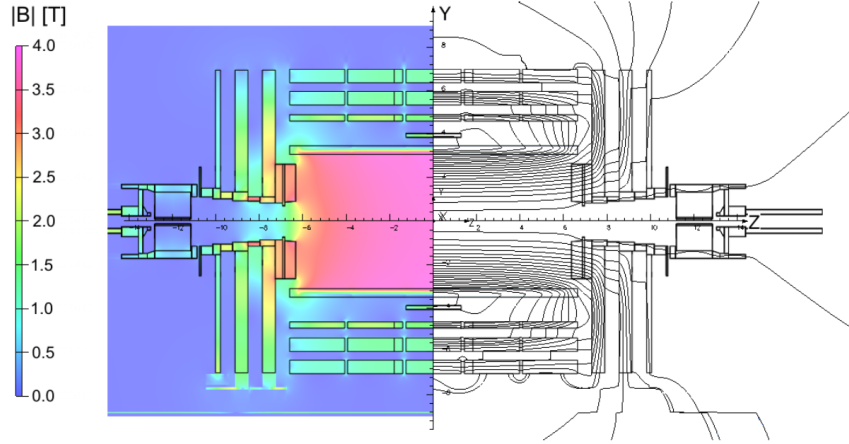


*Fig. 4.8:* Longitudinal slice of CMS detector while operating at 3.8-T central magnetic field. The right-hand side of the figure shows a mapping of the magnetic field lines while the left-hand side shows a mapping of the field strength. Reprint from [10]

320 (RPC). A cross-sectional view of the muon system along with the rest of the  
 321 CMS detector is shown in Figure 4.9.

322 The DT chambers are used barrel region for  $|\eta| < 1.2$ . Each chamber is  
 323 comprised of three superlayers which are made up of four staggered layers  
 324 of rectangular drift cells. Each of these drift cells contains a mixture of  
 325 Ar and CO<sub>2</sub> gases. An anode wire, located at the center of each tube, is  
 326 made of gold-plated stainless steel and is held at 3.6 kV. The gas is ionized  
 327 when a charged particle passes through and the resulting free electrons are  
 328 attracted to the anode wire. As these electrons pass through the gas they  
 329 cause further ionization which results in an electron avalanche. The layers  
 330 of drift cells are oriented in such a way that two of the three superlayers  
 331 give the muon position in the  $\phi$ -direction and one gives the position in the  
 332  $z$ -direction. The result is a spacial resolution of 77-123  $\mu\text{m}$  along the  $\phi$   
 333 direction and 133-193  $\mu\text{m}$  along the  $z$  direction for each DT chamber [14].

334 On the endcaps, covering the pseudorapidity range of  $0.9 < |\eta| < 2.4$ ,  
 335 are the CSCs. In this region there is a higher muon flux as well non-uniform  
 336 magnetic fields so this portion of the muon system must have higher gran-  
 337 ularity provided by the CSCs. Each of these chambers contain panels that  
 338 divide it into six staggered layers. The cathode strips are oriented along the  
 339  $r$ -direction to give position measurements in the  $\phi$ -direction while anode  
 340 wires run perpendicular in between the panels to give  $r$ -direction position

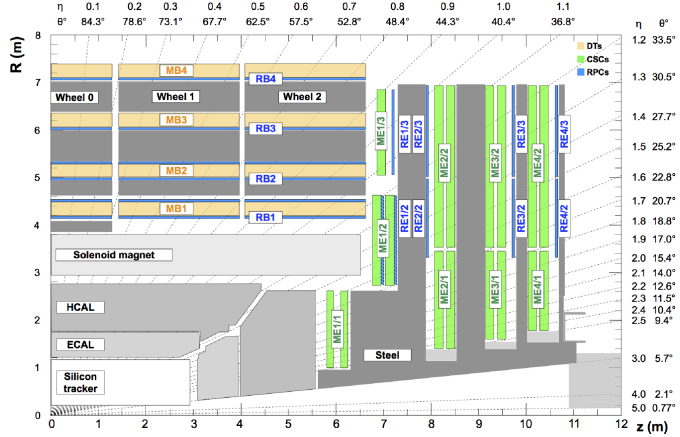


Fig. 4.9: Cross-section of one quadrant of the CMS detector. The DTs are labeled as "MB" (Muon Barrel) and the CSCs are labelled as "ME" (Muon Endcap). The RPCs are "RB" for those in the barrel and "RE" for those in the endcap. Reprint from [20].

341 measurements. The spacial resolution provided by the CSCs is 45-143  $\mu$ m  
 342 [20].

343 Both the endcap and barrel regions, spanning  $|\eta| < 1.6$ , contain RPCs to  
 344 provide more precise timing measurements. Each RPC is a gaseous parallel-  
 345 plate detector. High voltage is applied to two large plates which have a  
 346 layer of gas between them. Outside the chamber is an array of cathode  
 347 strips which is used to detect electron cascades resulting from muons passing  
 348 through and ionizing the gas. Where the DTs and CSCs provide precise  
 349 position information, the RPCs have a very fast response time which gives  
 350 a time resolution better than 3 ns [20]. This allows for the RPCs to be used  
 351 as a dedicated muon trigger that can insure each muon is assigned to the  
 352 correct bunch crossing.

353

## 5. MIP TIMING DETECTOR (MTD)

354

### 5.1 Introduction

355 In the coming years the LHC will be working toward upgrades that will  
 356 lead a substantial increase in luminosity. The timeline for future operations  
 357 of the LHC is shown in Figure 5.1. In 2019 the LHC entered a two-year  
 358 shutdown, Long Shutdown 2 (LS2). Upgrades of the LHC injector complex  
 359 to increase the beam brightness will take place during this shutdown. After  
 360 LS2 the LHC will enter Run 3 which will run for three years at 13-14 TeV. At  
 361 the completion of Run 3 the LHC will enter Long Shutdown 3 (LS3) which  
 362 will last approximately 2.5 years. During LS3 the optics in the interaction  
 363 region will be upgraded to produce smaller beams at the interaction point.  
 364 The completion of this upgrade will usher in the High Luminosity (HL-LHC)  
 365 era or Phase 2 of LHC operations, during which the combination of brighter  
 366 beams and a new focusing scheme at the IP allows for a potential luminosity  
 367 of  $2 \times 10^{35} \text{ cm}^{-2}\text{s}^{-1}$  at the beginning of each fill [5].

**LHC/ High-Luminosity LHC timeline**

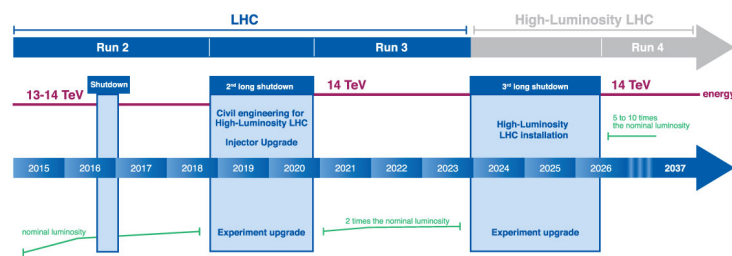


*Fig. 5.1: Timeline for LHC [15]*

368

The increased luminosity results in more interactions per bunch crossing or pileup. In order to limit the amount of pileup the experiments must

disentangle to more manageable levels, the nominal scenario would be operating at a stable luminosity of  $5.0 \times 10^{34} \text{ cm}^{-2} \text{ s}^{-1}$ . This would limit the pileup to an average of 140. The ultimate scenario for operations would be running at  $7.5 \times 10^{34} \text{ cm}^{-2} \text{ s}^{-1}$  which brings the average pileup up to 200. The CMS detector in its current state is not capable of dealing with  $\approx 140\text{-}200$  pileup. At this level of pileup the spacial overlaps of tracks and energy depositions would lead to a degradation in the ability to identify and reconstruct hard interactions. In order to preserve the data quality of the current CMS detector this increased pileup must be reduced to an equivalent level approximately equal to current LHC operations which is  $\sim 40$ . The collision vertices within a bunch crossing have an RMS spread of 180-200 ps in time. If the beam spot were to be sliced into consecutive snap shots of 30-40 ps then the pileup levels per snapshot would be approximately 40. The space-time reconstruction of a 200 pileup event is shown in Figure 5.2. The addition of timing information to the  $z$  position spreads apart the vertices that would otherwise have been merged together and indiscernible. In order to achieve this a detector dedicated to the precise timing of minimum ionizing particles (MIPs), the MTD, will be added to the CMS detector.

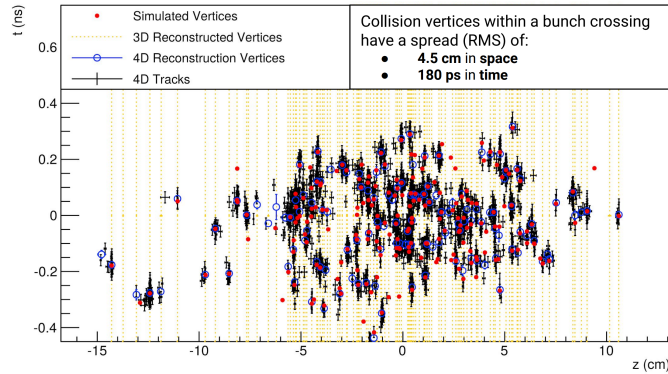


*Fig. 5.2:* Vertices from a simulated 200 pileup event. Need to replace this with the figure from the TDR.

388

## 5.2 Barrel Timing Layer

389 The Barrel Timing Layer (BTL) makes up the barrel region of the MTD.  
 390 It will provide pseudorapidity coverage up to  $|\eta| = 1.48$  with a geometric  
 391 acceptance of  $\sim 90\%$ . The BTL will be capable of detecting MIPs with a  
 392 time resolution of 30 ps at the start of Phase-2 operations and a luminosity-

<sup>393</sup> weighted time resolution of  $\sim 45$  ps when radiation damage effects are taken  
<sup>394</sup> into account.

## 6. CMS TRIGGER SYSTEM

396 When operating at nominal luminosity the LHC produces over 1 billion  
 397 proton-proton collisions per second. Finite computing speed and storage  
 398 capacity limit the rate at which CMS can record events to be about 1 kHz  
 399 [8]. Decreasing the rate from 1 GHz to 1 kHz is accomplished by using a  
 400 two-level trigger system to quickly decide which events will be discarded  
 401 and which will be recorded. The first stage is a hardware-based Level 1 (L1)  
 402 trigger and the second stage is software-based High Level Trigger (HLT).

### 6.1 *L1 trigger*

404 The L1 trigger decreases the rate by about six orders of magnitude from 1  
 405 GHz to 100 kHz by performing rough calculations on information from the  
 406 ECAL, HCAL, and muon subsystems using field-programmable gate arrays  
 407 (FPGAs). The L1 trigger can be divided further into the calorimeter and  
 408 muon triggers. The schematic of the L1 trigger system in Figure 6.1 shows  
 409 both the calorimeter and muon triggers. The calorimeter trigger trigger  
 410 uses information from the ECAL and HCAL subdetectors to construct pho-  
 411 ton, electron, and jet candidates in addition to quantities such as missing  
 412 transverse momentum and total hadronic activity. The muon trigger uses  
 413 information from all three muon subsystems to construct muon candidates.  
 414 The outputs from the calorimeter and muon triggers goes into the Global  
 415 Trigger (GT) which decides which events should be recorded and which are  
 416 to be discarded [21].

#### 6.1.1 *Calorimeter trigger*

418 Trigger Primitives (TP) are the raw inputs from the ECAL and HCAL  
 419 for the calorimeter trigger. The TP, which contain information regarding  
 420 the energy deposits in the calorimeters, are passed to the first layer of the  
 421 calorimeter trigger. This first layer consists of several FPGA cards that  
 422 receive data from several bunch crossings, but are each mapped to a section  
 423 of the detector. This data is then passed on to the second layer in such a way

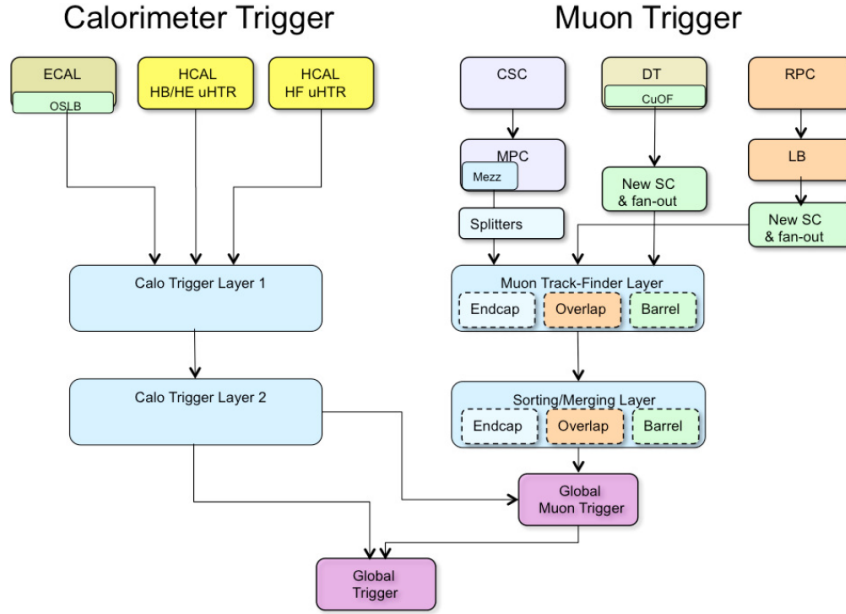


Fig. 6.1: L1 trigger system. Reprint from [3]

424 that each FPGA in this layer will receive data for the entire calorimeter for  
 425 each bunch crossing. Candidate objects are then constructed and organized  
 426 into a sorted list according to transverse momentum and passed on to the  
 427 GT and the global muon trigger.

#### 428           6.1.2 Muon trigger

429 TP for the muon trigger come from the three muon detectors, the CSCs,  
 430 DTs, and RPCs. These are then passed on to the first layer of the muon  
 431 trigger (Muon Track-Finding Layer) where the TP are combined to recon-  
 432 struct muon tracks for sections of  $\phi$  for different regions of  $|\eta|$ . The barrel  
 433 track-finder for  $|\eta| < 0.83$ , the endcap track-finder for  $|\eta| > 1.24$ , and the  
 434 overlap track-finder for  $0.83 < |\eta| < 1.24$ . This data is passed on to the  
 435 second layer where the sections of  $\phi$  are merged and subsequently passed  
 436 on to the global muon trigger where it is combined with the output from  
 437 Calo Trigger Layer 2 to compute isolation. The global muon trigger then  
 438 combines the  $\eta$  regions and passes a list of the top eight muon candidates  
 439 to the GT.

---

 440                   6.1.3 Global Trigger

441 Final processing of the reconstructed objects and quantities constructed by  
 442 the calorimeter and muon triggers is carried out by the GT. L1 algorithms  
 443 or "seeds" are implemented by the GT using these objects. A full set of L1  
 444 seed is called a L1 menu and can be adjusted to meet the requirements of  
 445 the CMS physics program. Each L1 seed can be given a "prescale", which is  
 446 an integer value  $N$  that can be used to reduce the rate of a particular trigger  
 447 path. This is done by only applying the trigger to one out of  $N$  events and  
 448 can be used to take advantage of the current LHC running conditions.

## 449                   6.2 High Level Trigger

450 Events that are accepted by the L1 trigger are passed on to the HLT which  
 451 is based in software and is therefore capable of analyzing events with a higher  
 452 degree of sophistication. The HLT has access to information from the full  
 453 detector and implements "paths" to select events of interest from those pass-  
 454 ing the L1 trigger. Each HLT path is a set of criteria that is used to either  
 455 accept or reject an event. The full set of HLT paths is the HLT menu. Each  
 456 HLT path is "seeded" by one or more L1 seeds in order to decrease comput-  
 457 ing time. That means that a given HLT path will only be processed if the  
 458 L1 bits associated with its seed or seeds fire. Each HLT path is assigned to  
 459 a primary dataset depending on its general physics signature. In the case  
 460 of this analysis, the primary dataset used for signal events was DoubleEG  
 461 for years 2016 and 2017. This was merged into the EGamma dataset for  
 462 2018. The SingleMuon dataset was used for trigger efficiency studies. A list  
 463 of the primary HLT used for each year along with its associated primary  
 464 dataset is listed in Table 6.1. The HLT path for 2016 is different because  
 465 HLT\_DoublePhoton70 was not a part of the HLT menu until 2017.

Tab. 6.1: Primary HLT

Year	HLT path	Primary dataset
2016	HLT_DoublePhoton60	DoubleEG
2017	HLT_DoublePhoton70	DoubleEG
2018	HLT_DoublePhoton70	EGamma

## 466                   6.3 Trigger efficiency

467        7. CMS PARTICLE AND EVENT RECONSTRUCTION

468        After an event is chosen to be stored by the trigger system, the output from  
469        all of the sub-detectors is saved and recorded to disk as "RAW" data. These  
470        data contain information about the response of each sub-detector, such as  
471        tracker hits and energy deposition in the calorimeters. As was mentioned  
472        in Chapter 4, shown in Table 4.1 and Figure 4.2, the CMS was designed  
473        such that each type of particle resulting from the  $pp$  collisions at the IP  
474        would leave a distinct signature in the sub-detectors. This allows for the  
475        information to be reconstructed into lists of physics object candidates such  
476        as photons, electrons, muons, etc and quantities such as missing transverse  
477        momentum. The particle flow (PF) algorithm performs this reconstruction  
478        by first building tracks and calorimeter clusters. These two elements are the  
479        inputs to the reconstruction of the aforementioned physics object candidates  
480        using a "link" algorithm.

481                  7.1    *Tracks*

482        A combinatorial track finder algorithm based on the Kalman filtering tech-  
483        nique uses the hits in the silicon tracker to reconstruct tracks of charged  
484        particles [17]. Each iteration of the algorithm is comprised of three steps:

- 485        • Seed generation: Find a seed consisting of two to three hits that is  
486        compatible with a track from a charged particle.
- 487        • Track finding: Use pattern recognition to identify any hits that are  
488        compatible with the trajectory implied by the seed generated in the  
489        first step.
- 490        • Track fitting: Determine the properties of the track, such as origin,  
491        trajectory, and transverse momentum by performing a global  $\chi^2$  fit.

492        The first iteration uses stringent requirements on the seeds and the  $\chi^2$   
493        of the track fit to pick out isolated jets which have very high purity. The  
494        hits associated with these high purity tracks are then removed to reduce the

495 combinatorial complexity for subsequent iterations. This allows successive  
 496 iterations to identify less obvious tracks by progressively loosening criteria  
 497 while the removal of previously associated hits mitigates the likelihood of  
 498 fake tracks being built.

## 499 7.2 Calorimeter clusters

500 Calorimeter clusters are constructed using energy deposition information  
 501 from the calorimeters. Clusters are formed by first identifying the seed cell  
 502 (ECAL crystal or HCAL scintillating tile) that corresponds to the local  
 503 maxima of an energy deposit that is above a given threshold. Neighboring  
 504 cells are then aggregated to grow topological clusters if their signals are  
 505 above twice the standard deviation of the level of electronic noise.

## 506 7.3 Object identification

507 At this point the tracks and calorimeter clusters are linked to form a PF  
 508 block. This linkage is done with an algorithm that quantifies the likelihood  
 509 that a given track and cluster were results of the same particle. As PF blocks  
 510 are identified as object candidates they are removed from the collection prior  
 511 to each subsequent iteration until all tracks and clusters have been assigned  
 512 to a PF object candidate. The following sections will outline how each of  
 513 these PF objects is identified.

### 514 7.3.1 Muons

515 Muons are the easiest particle to identify, so they are the first objects recon-  
 516 structed in the CMS. PF Muons are classified in three categories depending  
 517 on how their tracks are reconstructed:

- 518 • Tracker muons: Tracks reconstructed from the inner tracker having  
 519  $p_T > 0.5$  GeV and  $|\vec{p}| > 2.5$  GeV that, when propagated to the muon  
 520 system, match at least one hit in the muon chambers.
- 521 • Stand-alone muons: Tracks reconstructed only using hits in the muon  
 522 system.
- 523 • Global muons: Stand-alone muons that coincide with a track from the  
 524 inner tracker.

525 After a muon is reconstructed it is given an identification or ID based on  
 526 observables such as the  $\chi^2$  of the track fit, how many hits were recorded

527 per track, or how well the tracker and stand-alone tracks matched. These  
528 IDs represent different working points (loose, medium, and tight) which  
529 correspond to increasing purity but decreasing efficiency as you move from  
530 loose toward tight.

531 **7.3.2 Electrons**

532 The next objects reconstructed in the CMS are electrons. Bremsstrahlung in  
533 the tracker layers causes substantial energy loss and changes in momentum  
534 which requires the use of a dedicated tracking algorithm. In place of the  
535 Kalman filtering technique, a Gaussian-sum filter (GSF) algorithm is used.  
536 This algorithm uses a weighted sum of Gaussian PDFs which does a bet-  
537 ter job of modeling the Bremsstrahlung effects than the Kalman filtering  
538 technique which uses a single Gaussian PDF.

539 PF ECAL clusters are regrouped by identifying a seed cluster then asso-  
540 ciating and adding clusters from Bremsstrahlung photons to form superclus-  
541 ters. The schematic in Figure 7.1 shows how the Bremsstrahlung photons  
542 are emitted in directions tangent to the trajectory of the electron. Electrons  
543 bending in the magnetic field causes spreading of PF ECAL clusters to typ-  
544 ically occur along the  $\phi$ -direction. Two approaches are used to associate  
545 the superclusters to GSF tracks. One is the ECAL-driven method, which  
546 uses superclusters with  $p_T > 4$  GeV as seeds for the GSF track finding al-  
547 gorithm. This works well for high- $p_T$  isolated electrons because the bend  
548 radius is less severe which decreases the spread of the PF ECAL clusters.  
549 This results in more of the Bremsstrahlung radiation being recovered and  
550 correctly associated with an electron candidate. The second approach is the  
551 tracker-driven method which uses tracks with  $p_T > 2$  GeV as seeds that are  
552 propagated out to the surface of the ECAL and used for clustering. This  
553 method works best with soft electrons like those in jets because it relies on  
554 the high granularity of the tracker to disentangle overlapping energy deposits  
555 in the ECAL. [18]

556 As a final step, a boosted decision tree (BDT) is used to discriminate  
557 between real and fake electrons. The BDT is given variables associated with  
558 track-cluster matching, shower shape, and tracking. The output score of  
559 the BDT is used to classify electrons into loose, medium, and tight working  
560 points which exhibit the same purity and efficiency trends as the muon  
561 working points.

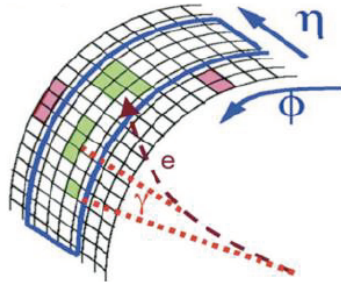


*Fig. 7.1: Effect of Bremsstrahlung*

562

### 7.3.3 Photons

563 Unlike electrons, photons typically deposit most of their energy in the ECAL  
 564 without interacting with the tracker therefore their reconstruction is seeded  
 565 from ECAL superclusters that do not have any GSF tracks associated with  
 566 them. The goal of the clustering algorithm for photon reconstruction is to  
 567 include all of the energy deposits of electrons from photon conversions. As  
 568 with the calorimeter clustering algorithm, the photon clustering starts by  
 569 identifying a local energy maxima as a seed crystal. In the EB a cluster is  
 570 made up of several parallel strips of crystals  $5 \times 1$  in  $\eta \times \phi$ . The first strip  
 571 has the seed crystal at its center. Neighboring strips in the  $\phi$ -direction are  
 572 added if they have energy above a threshold of 10 GeV but less than that of  
 573 the subsequent strip with a maximum of 17 strips in a cluster.

574

### 7.3.4 Jets

575

## 7.4 Missing transverse momentum

## 8. DATA ANALYSIS

### 8.1 Overview

### 8.2 Data sets

### 8.3 Object definitions

## BIBLIOGRAPHY

- [1] *The CMS electromagnetic calorimeter project: Technical Design Report.* Technical design report. CMS. CERN, Geneva, 1997.
- [2] *The CMS hadron calorimeter project: Technical Design Report.* Technical design report. CMS. CERN, Geneva, 1997.
- [3] CMS Technical Design Report for the Level-1 Trigger Upgrade. 6 2013.
- [4] S. Abdullin et al. The CMS barrel calorimeter response to particle beams from 2-GeV/c to 350-GeV/c. *Eur. Phys. J. C*, 60:359–373, 2009. [Erratum: Eur.Phys.J.C 61, 353–356 (2009)].
- [5] G. Apollinari, O. Brüning, T. Nakamoto, and Lucio Rossi. High Luminosity Large Hadron Collider HL-LHC. *CERN Yellow Rep.*, (5):1–19, 2015.
- [6] S Baird. Accelerators for pedestrians; rev. version. Technical Report AB-Note-2007-014. CERN-AB-Note-2007-014. PS-OP-Note-95-17-Rev-2. CERN-PS-OP-Note-95-17-Rev-2, CERN, Geneva, Feb 2007.
- [7] David Barney. CMS Slice. Feb 2015.
- [8] L. Cadamuro. The CMS Level-1 trigger system for LHC Run II. *JINST*, 12(03):C03021, 2017.
- [9] Jean-Luc Caron. Cross section of lhc dipole.. dipole lhc: coupe transversale. ”AC Collection. Legacy of AC. Pictures from 1992 to 2002.”, May 1998.
- [10] S Chatrchyan et al. Precise Mapping of the Magnetic Field in the CMS Barrel Yoke using Cosmic Rays. *JINST*, 5:T03021, 2010.
- [11] CMS Collaboration. CMS Technical Design Report for the Pixel Detector Upgrade. Technical Report CERN-LHCC-2012-016. CMS-TDR-11, Sep 2012. Additional contacts: Jeffrey Spalding, Fermilab, Jef-

- frey.Spalding@cern.ch Didier Contardo, Universite Claude Bernard-Lyon I, didier.claude.contardo@cern.ch.
- [12] CMS Collaboration. Description and performance of track and primary-vertex reconstruction with the CMS tracker. *JINST*, 9(CMS-TRK-11-001. CERN-PH-EP-2014-070. CMS-TRK-11-001):P10009. 80 p, May 2014. Comments: Replaced with published version. Added journal reference and DOI.
  - [13] The CMS Collaboration. The CMS experiment at the CERN LHC. *Journal of Instrumentation*, 3(08):S08004–S08004, aug 2008.
  - [14] The CMS collaboration. The performance of the CMS muon detector in proton-proton collisions at  $\sqrt{s}=7$  TeV at the LHC. *Journal of Instrumentation*, 8(11):P11002–P11002, nov 2013.
  - [15] Cinzia De Melis. Timeline for the LHC and High-Luminosity LHC. Frise chronologique du LHC et du LHC haute luminosité. Oct 2015. General Photo.
  - [16] Lyndon Evans and Philip Bryant. LHC machine. *Journal of Instrumentation*, 3(08):S08001–S08001, aug 2008.
  - [17] R. Fruhwirth. Application of Kalman filtering to track and vertex fitting. *Nucl. Instrum. Meth. A*, 262:444–450, 1987.
  - [18] Jonas Rembser. CMS Electron and Photon Performance at 13 TeV. *J. Phys.: Conf. Ser.*, 1162(1):012008. 8 p, 2019.
  - [19] Tai Sakuma and Thomas McCauley. Detector and event visualization with SketchUp at the CMS experiment. *Journal of Physics: Conference Series*, 513(2):022032, jun 2014.
  - [20] A.M. Sirunyan et al. Performance of the CMS muon detector and muon reconstruction with proton-proton collisions at  $\sqrt{s}=13$  TeV. *Journal of Instrumentation*, 13(06):P06015–P06015, jun 2018.
  - [21] J. Wittmann, B. Arnold, H. Bergauer, M. Jeitler, T. Matsushita, D. Rabady, B. Rahbaran, and C.-E. Wulz. The upgrade of the CMS global trigger. *Journal of Instrumentation*, 11(02):C02029–C02029, feb 2016.